SLAM-aided forest plot mapping combining terrestrial and mobile laser scanning

Jie Shao, Wuming Zhang, Nicolas Mellado, Nan Wang, Shangshu Cai, Lei Luo, Thibault Lejemble, Guangjian Yan, Shuangna Jin

SLAM-aided forest plots mapping combining terrestrial and mobile laser scanning

Jie Shao [1,2], Wuming Zhang [3,4] , Nicolas Mellado [2,5], Nan Wang [6], Shangshu Cai[1], Lei Luo [7], Thibault Lejemble [2], Guangjian Yan[1] Shuangna Jin[1]

1. BNU - Beijing Normal University (No. 19, XinJieKouWai St., HaiDian District, Beijing 100875, P. R. China - Chine)
2. IRIT - Institut de recherche en informatique de Toulouse (118 Route de Narbonne, F-31062 Toulouse Cedex 9 - France)
3. ICJ - Institut Camille Jordan [Villeurbanne] (Bât. Jean Braconnier 43 bd du 11 novembre 1918 69622 VILLEURBANNE CEDEX - France)
4. SYSU - Sun Yat-Sen University [Guangzhou] (135 Xingang W Rd, Haizhu, Guangzhou, Guangdong, China - Chine)
5. CNRS - Centre National de la Recherche Scientifique
6. Wuhan Polytechnic University (Foreign Affairs Office 68 Xuefu South Road, Changqing Garden, Wuhan 430023, Hubei, China - Chine)
7. National University of Defense Technology [China] (Hunan, Changsha, Kaifu - Chine)

Abstract

Precise structural information collected from plots is significant in the management of and decision-making regarding forest resources. Nowadays, laser scanning is widely used in forestry inventories to acquire precise three-dimensional (3D) structural information, e.g. tree stem diameters at multiple height. Currently, there are three main data acquisition methods in ground-based forest measurements: single-scan terrestrial laser scanning (TLS), multi-scan TLS and mobile laser scanning (MLS). Nevertheless, each of these methods causes specific difficulties for forest measurements. Due to occlusion effects, single-scan TLS provides scan for only one side of trees. Multi-scan TLS overcomes occlusion problems, however at the cost of longer acquisition time, human labor, and requires more efforts in data preprocessing. These problems in TLS methods are largely avoided with MLS, however the geometrical peculiarity of forests (e.g. similarity between tree shapes, placements and occlusion) complexities the motion estimation and reduces mapping accuracy.

Therefore, this paper proposes a novel method combining single-scan TLS and MLS for forest 3D data acquisition. We use single-scan TLS data as a reference, onto which we register MLS point clouds, so they fill up the omission of the single-scan TLS data. To register MLS point clouds on the reference, we extract virtual feature points that are sampling the trees stem centerlines, and propose a new optimization-based registration framework. In contrast to previous studies of MLS-based, the proposed method exploits sufficiently the natural geometric characteristics of trees. We demonstrate the effectiveness, robustness, and accuracy of the proposed method on three forest plots, from which we extract structural information. The experimental results show that the omission of tree stem data caused by one scan can be compensated for by the MLS data, and the time of the field measurement is much less than that of the multi-scan TLS mode. In addition, single-scan TLS data provides a strong global constraint for the MLS-based forest mapping, which allows reaching a low mapping error, e.g., approximately 1.5 cm mean errors in the horizontal direction of the test plots, with standard deviations at the millimeter level, and approximately 2 cm mean errors in the vertical direction.

Keywords: Forest mapping; LiDAR; SLAM; Single-scan TLS; MLS

1. Introduction

Precise measurements of forest structures are crucial for the management of and decision-making regarding forest resources, studies of ecosystem processes and biodiversity, and so on (Spies, 1998). However, accurate forestry measurements are not straightforward because of the complexity of forests. Some conventional, simple tools (e.g.,

calipers and clinometers) have been used in forest field measurements, but these measurement methods are widely recognized as time consuming, laborious and expensive. The situation has been changing in the last two decades due to the development of light detection and ranging (LiDAR), which has the major advantage of automatically and rapidly documenting the three-dimensional (3D) forest spaces in forestry inventories at millimeter-level details (Hyyppä, 2000; Næsset 2011; Newnham et al., 2015; Torresan et al., 2018). In this context, LiDAR-based 3D data acquisition has become one of the means of obtaining accurate forest measurements.

Terrestrial laser scanning (TLS), also known as ground-based LiDAR, has been suggested to be a practical option to quickly provide accurate and nondestructive estimations of forest biophysical metrics (Latifi et al., 2015; Stovall et al., 2017; Wilkes et al., 2017). Compared to conventional manual measurements, it has also shown a higher work efficiency in forestry inventories (Murphy et al., 2010). 3D data acquisition is an essential prerequisite and is the key to digital forest measurements. Two data acquisition modes have been reported frequently in TLS-based field measurements: single-scan and multi-scan.

In single-scan mode, the scanner is placed at a single point in the forest sample plot and allows the acquisition of only one side of the visible trees (Astrup et al., 2014). Single-scan mode has a simpler data acquisition setting and faster measuring speed of the two modes, e.g., it can typically measure a plot within 20 minutes (Liang et al., 2016). However, occlusion effects from the forest objects (e.g., trees, branches, and ground vegetation) in the direction of the laser beams cause a low detection rate in forest measurements, e.g., from 0% and 46% depending on the plot size and the forest type (Mass et al., 2008; Lovell et al., 2011; Liang et al., 2012; Trochta et al., 2013; Mengesha et al., 2015). Consequently, multiple scans are often necessary to observe all the trees in the sample plot. In multi-scan mode, the scanner observes a sample plot from multiple positions, which gives it the potential to detect all trees and provides full coverage of a stem surface. This mode is considered the most accurate for forest mapping. Unfortunately, it requires more time and laborious field measurements and more data preprocessing. Depending on plot size and the forest type, multi-scan mode typically takes one to ten hours to measure a sample plot, which includes determining the location and distribution of the scanners and reference targets and performing multiple scans, for example, the TLS-based field measurement usually takes at least one hour in a forest plot with size of 30 m × 30 m and approximately ten hours in a sample plot with size of 100 m × 100 m. In addition, the cost of manual or semiautomated registration of multiple scans limits its practicality. For instance, placing reflective targets in forest environments is tedious because most related methods evenly distribute targets in positions that can be seen from multiple viewpoints and require additional user interactions to identify undetected targets (Pueschel, 2013; Calders et al., 2014; Cifuentes et al., 2014). Recently, mobile laser scanning (MLS) has gained attention in forest mapping because of the advantage of the immensely faster data collection in comparison to the TLS modes (Liang et al., 2014), e.g., it can measure small forest sample plots within a few minutes.

Therefore, this paper proposes a novel SLAM method combining single-scan TLS point cloud and MLS point clouds for forest environments. The method addresses the global consistency problem and maintains the accuracy of forest mapping without the GNSS-IMU system, even in the case of trajectory discontinuity and without loop closures. To solve the occlusion and object similarities problem, we propose combining virtual feature points that represent the tree stem center and real, evenly distributed feature points in forest plot mapping, which allows the mapping of forest point clouds with low overlap and prevents errors caused by inaccurate corresponding pairs in forest environments. Following the introduction section, Section 2 summarizes the related work first. The key steps of the proposed method is elaborated in Section 3. Section 4 introduces the materials and the performances of the proposed method on field measurements and then discusses the advancements of the proposed method, after which discussions are presented and conclusions are drawn at the end.

2. Related work

The main limitation of MLS appears during the mapping step, where each MLS point cloud is mapped on the point clouds acquired in the previous time steps. Most of the existing MLS-based mapping techniques are based on Global Navigation Satellite System/Inertial Measurement Unit (GNSS-IMU)-based techniques. In that setup, the GNSS maintains the global position accuracy, and the IMU provides attitude information for the orientation of the laser scanner. In contrast to road and urban contexts, the occlusion of trees and vegetation often weakens or blocks the GNSS signal and prevents to the mapping. In such cases, the location of the MLS point cloud needs to be estimated during the mapping step, which leads to the so-called *simultaneous localization and mapping* (SLAM) problem (Dissanayake et al, 2001).

The common SLAM techniques involve the filter-based and graph-based methods. In the filter-based method, Extended Kalman Filter (EKF) (e.g., Hector SLAM) (Kohlbrecher et al., 2011) and Particle Filters (PF) (e.g., G-mapping) (Grisetti et al., 2007) are the common filters for SLAM technology. The related EKF and PF methods rely on strong assumptions about the robot motion model and the sensor noise, and generally only consider motion relationship between adjacent data. When the assumptions are violated or loop-closure is executed, the filter-based methods will be difficult to address; in addition, as the scenario expands, the filter-based method will increase the memory consumption and computation. Graph-based methods are popular in the SLAM community, as they solve both the position and mapping problems by combining poses of scanner and constraint relationships between these poses. For example, Karto-SLAM (Konolige et al., 2010) and Cartographer (Hess, et al., 2016) calculate pose of scanner at different time and execute loop closure detection to construct pose graph, and then eliminate cumulative error by optimizing the pose graph. Because only the pose optimization of scanner is considered, the methods can achieve low computational resource consumption and even real-time optimization. However, this kind of method has difficulty obtaining highly accurate position and mapping results, which is difficult to meet the requirements of high-precision forest measurements. In contrast, another graph-based method, bundle adjustment (BA), is widely used for solving the SLAM problem (Mouragnon et al., 2009). The BA method optimizes simultaneously the object features and the pose of the scanner using nonlinear optimization, which strongly relies on the matching features and can obtain highly accurate mapping results. For instance, the LOAM method (Zhang and Singh, 2014) selects line and plane features on objects surfaces to estimate the motion of the scanner and obtained highly accurate mapping results in indoor and urban scenarios where consist of stable and distinct features. However, due to complexity and similarity of object in forests, the reliable features are difficult to extract from object surface, and inaccurate corresponding pairs can fall scan matching into a local optimum. Moreover, another challenge in SLAM is to avoid error accumulation during data acquisition, i.e., by considering global optimization (Grisetti et al., 2010). Several methods maintain global position accuracy by performing multiple loop-closure detections (Mur-Artal, et al., 2015), generally increasing the complexity of the algorithm (Labbé and Michaud, 2014). Other studies achieve global optimization using prior information. For example, Kukko et al. (2017) used graph-based SLAM to correct the GNSS-IMU trajectory for position drift and in turn, the initial trajectory that obtained from the GNSS-IMU system was regarded as prior information and provided the constraints for the graph SLAM. The method not only achieved forest mapping, but also improved the absolute positioning accuracy; however, the GNSS signal loss caused by the occlusions of trees may affect the performance in practice. In addition, aerial image (Kümmerle et al., 2011; Javanmardi et al., 2017) and sketch map (Shah and Compbell, 2013; Behzadian et al., 2015; Mielle et al., 2018) are usually used to generate constraints for SLAM-based mapping, and the related methods showed reliability of prior information in indoor and urban scenarios (Wang et al., 2018). However, aerial images are difficult to provide constraints for below-canopy forest mapping due to the occlusions of canopy; in addition, the methods based on sketch maps have difficulty meeting mapping requirements for high-precision forest measurements. Consequently, the complex and irregular

forest environments pose problems to the existing SLAM methods.

A key step of most SLAM system is the registration step, where pairs of input scans are matched and aligned. This process is known as point-cloud registration, a topic studied for decades with a wide range of approaches proposed in the general setting (Mitra et al. 2004, Rusu et al. 2008, Mellado et al. 2014, Pomerleau et al. 2015). In this work, we focus on forest mapping and restrict our review to this application case. A first type of approaches uses artificial markers placed in the scene, e.g., reflective tape, retroreflective spheres, and reflectors (Henning and Radtke, 2006; Hilker et al., 2012; Zhang et al., 2016a). These markers serve as precise and unambiguous tie points for achieving highly accurate point cloud registration. Nevertheless, placement of artificial markers is generally time consuming and labor intensive in forest environments, and the related studies commonly focus on several dense point cloud (e.g., TLS data). Extracting markers from sparse MLS data is however more difficult due to the size of markers and the effects of occlusion, and might also be impractical for thousands of MLS point clouds. In contrast, marker-free registration methods aim at registering the scans without markers,. A first category of approaches detect geometric features that play the role of digital markers. For example, Kelbe et al. (2016) regarded stem-terrain intersection points as matching features and generated tie point triplets for registration of TLS data, Polewski et al. (2019) used the tree positions to achieve marker-free registration of point clouds. A second category of approaches use descriptor-free registration methods, see for instance the study by Theiler et al., (2014-1) on the use of congruent set registration for, among other application cases, forest registration. The aforementioned methods commonly focus on coarse registration and need a fine registration step in post-process. The Iterative Corresponding point (ICP) (Besl and Mckay, 1992) is nowadays the standard approach for local registration. It starts by computing correspondances between pairs of points-clouds, and then minimize the distance between those corresponding pairs. Normal distributions transform (NDT) (Magnusson et al., 2007) is also often considered. In the NDT method, point cloud is represented by local normal distributions that are subdivided into a grid of cell; then, search of closest normal distribution is used to replace iterating over a whole point cloud. The two methods generally need a certain point clouds overlap to maintain the registration accuracy and are suitable for the scenarios with strong anti-density interference abilities, e.g., indoor and urban. However, forests exhibit strong auto-similarities (e.g. the trees stems are often very similar), which may confuse these approaches. When the distance between scan locations is large, inaccurate corresponding pairs are easily generated by the methods and cause inaccurate registration results, especially in registration of tree stems (Fig. 1). Therefore, the selection of feature brings challenges for scan matching in forest environments.

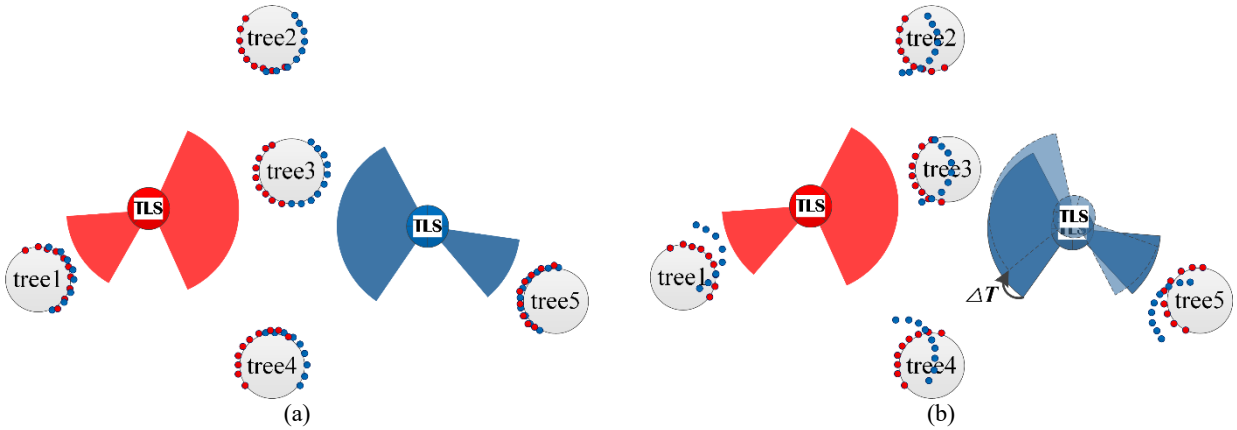

Fig. 1. The existing methods generally fail in forest environments because of the inaccurate corresponding pairs. The overlapping rates tree 1 and tree 5 are high; the overlapping rates in tree 2, tree 3, and tree 4, are low, especially in tree 3. The result (b) will replace result (a) when applying the traditional methods of point clouds registration.

3. Methods

3.1 Overview of the method

The goal of this paper is to realize forest plot mapping combining single-scan TLS data and MLS data. In this paper, we solve the problem in two steps: LiDAR odometry and global optimization (see Fig. 2).

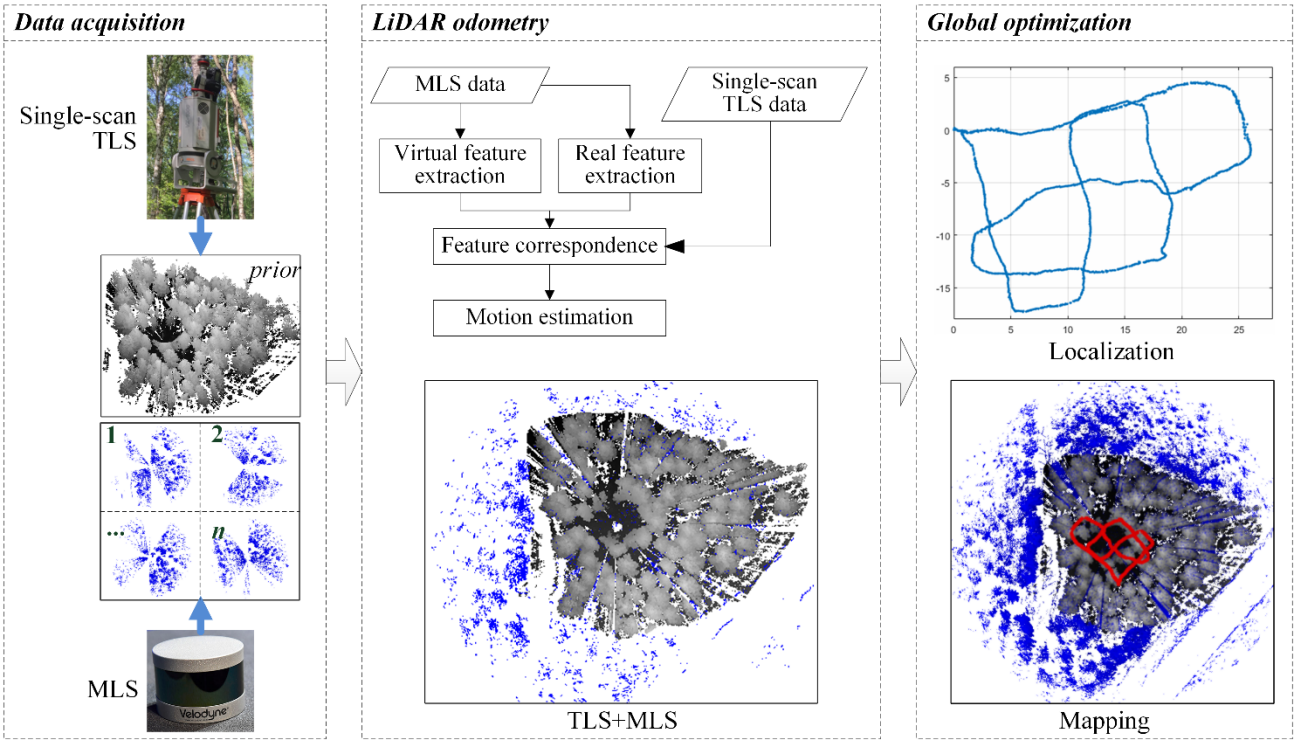

Fig. 2. Flowchart of Forest-SLAM.

(1) Odometry: estimate the motion of each frame MLS point cloud relative to the single-scan TLS data:

i. Feature extraction: extract feature points from each frame MLS point cloud. We distinguish between *virtual* features, which sample the reconstructed tree stem centerlines, and *real* features, which evenly sample the point cloud. In this paper, virtual features are points that are not part of the input point clouds and thus cannot be directly extracted from them, and the points that can be directly extracted from the point cloud are defined as real features. A layered clustering method is proposed for virtual feature extraction, and *difference of Gaussian* (DoG) method is used to extract real features.

ii. Feature correspondence: *virtual* and *real* feature points are matched between the reference single-scan TLS point cloud and each MLS point cloud by a nearest neighbor search.

iii. Motion estimation: the pose of each MLS point cloud is optimized with respect to the reference single-scan TLS point cloud by nonlinearly minimizing the corresponding feature point distances.

(2) Global optimization: simultaneously optimize the pose of all the MLS point clouds. The coordinate system of the reference single-scan TLS point cloud can be considered a global coordinate system and defines a global constraint for estimating the trajectory of the MLS device. We use a global incremental map without a loop closure to optimize the pose of all the MLS point clouds.

3.2 LiDAR odometry

LiDAR odometry is used to estimate the motion of the MLS system. In this paper, it is used to calculate the

transformation between the MLS point cloud and the reference. To reduce the cost of field measurement and extract accurate corresponding pairs, we propose combining two types of features, virtual features and real features, for LiDAR odometry. Before solving the MLS-based SLAM problem in forest, we firstly set certain conditions:

- The single-scan TLS point cloud is set as the reference, and the coordinate system is known to be the world coordinate system $\{W\}$. The coordinate system of each MLS point cloud is set to a local coordinate system $\{L\}$. $\{W\}$ and $\{L\}$ follow the right-hand rule.
- Let M_n and Γ_{TLS} be the MLS point cloud at the time of sweep n and the TLS point cloud, respectively.

The NDT algorithm only considers the probability distribution of points, so it does not take much time to search for matching features and has a certain stability; thus, it is used to provide the initial transformation for the following LiDAR odometry. Let $\tilde{M}_n^W$ be the reprojected point cloud based on the NDT.

3.3.1 Feature extraction

The NDT algorithm can obtain an initial transformation between the MLS point cloud and the reference, but there are obvious deviations in tree stem registration, especially in the horizontal direction (see Fig. 3). Therefore, a constraint that combines the virtual features and real features is proposed to reduce the stem position deviation.

(1) Extraction of virtual features

In forestry inventories, in practice, we generally assume that the cross sections of tree stems are approximately circular (Polewski et al., 2017) and that the shortest distance from the geometric center of the tree stem cross section to the surface of the tree stem equals the radius of the circle. It is obvious that these assumptions provide horizontal constraints. Therefore, we use geometric centers of tree stems as horizontal constraints for the registration of the MLS point cloud and the single-scan TLS data. In this paper, virtual features are points that cannot be directly extracted from point clouds. Thus, the centers of tree stems are defined as virtual features.

In this paper, we extract virtual features based on the layered clustering method. First, we divide each MLS point cloud into 16 subsets according to the vertical angular resolution. Then, the continuous and adjacent points in each subset are clustered based on connected-component labeling algorithm (Zhang et al., 2019). If the distance between the two farthest points in a cluster is greater than the maximum DBH or less than the minimum DBH in the plot, then the cluster will be removed. Finally, the circle fit based on the least squares method is used to detect the centers from these retained clusters. Furthermore, the centers that are continuously distributed in the vertical direction are used as virtual feature (see Fig. 3). Let V_n^L be the set of virtual features at the time of sweep n ($V_n^L \subset M_n$) and $\tilde{V}_n^W$ be the reprojected point sets based on the initial transformation. In addition, let r_{V_n} be the set of radius corresponding to the features.

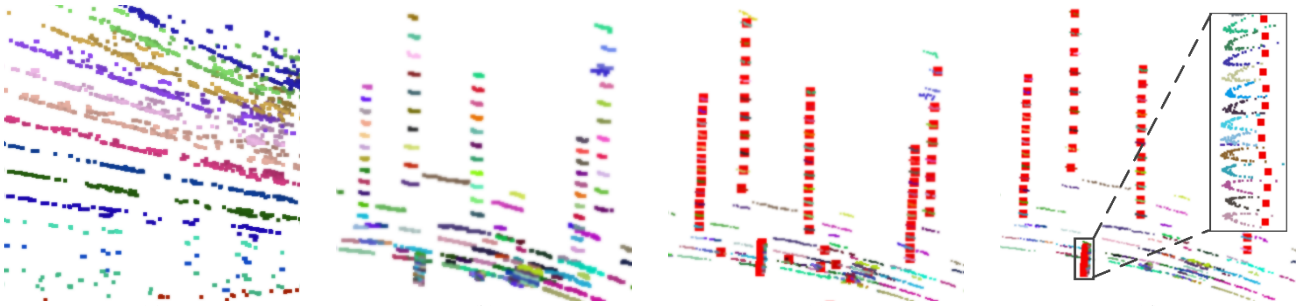

(a) (b) (c) (d)

Fig. 3. Extraction of virtual features. (a) Layered processing, different colors represent subsets on different layers. (b) Retaining cluster points. (c) Fitting the circle which radius is less than half of the maximum DBH (red points) and detecting its center. (d) Determining virtual features (bigger red points).

(2) Extraction of real features

Although virtual features can reduce the deviations in the horizontal direction, it is difficult to provide a constraint in the vertical direction because the tree stems are generally parallel in the vertical direction. However, those features that are evenly distributed in point cloud can provide an overall registration constraint. In this paper, we use the DoG algorithm to extract real features.

The DoG algorithm is a feature enhancement and extraction algorithm in digital image processing. The major advantages of features extracted by the DoG algorithm are their invariance to scaling, rotation and translation. Many high-contrast edges in two dimensions are on object silhouettes and have depth discontinuities, leading to unstable features across viewpoints. Nevertheless, 3D extraction could avoid such unstable feature points that highly contrast with their spatial neighbors, so this paper directly extracts the real features in 3D (Theiler et al., 2014-2). The principle of DoG-based 3D feature extraction is subtracting one blurred point cloud level from another blurred point cloud level. The blurred levels are obtained by convolving the point cloud with Gaussian kernels that have different standard deviations. In practice, to access to data easily, all raw MLS point clouds are first stored in depth maps; then, to reduce the impact of noise or outliers, we calculate the spatial distance between every point and its neighboring points. If the distance is large, the point will be tagged as noise or outlier and removed. Final, let R_n^L be set of real features at the time of sweep n ($R_n^L \subset M_n$) and $\tilde{R}_n^W$ be the reprojected point sets based on the initial transformation. The result is shown in Fig. 4.

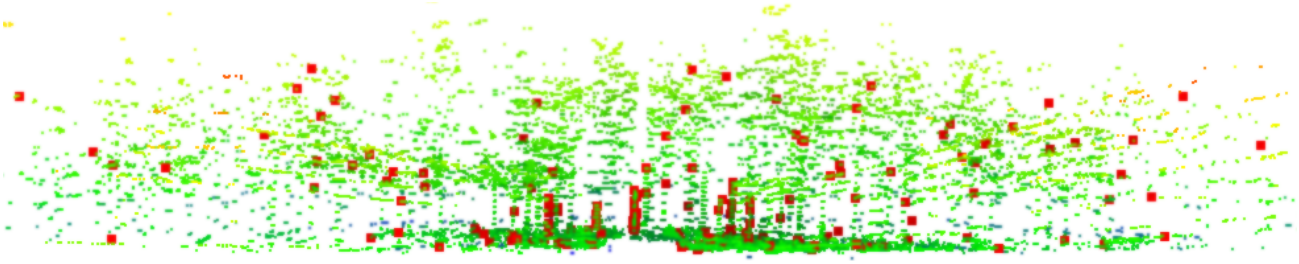

Fig. 4. Extraction of real features. Green points are the MLS data. Red points are real feature points, and 180 real feature points were extracted from each MLS point cloud.

3.3.2 Feature correspondence

Feature correspondence is used to search for corresponding virtual feature pairs and real feature pairs from the MLS and the single-scan TLS data and to estimate the motion of the MLS system in the global coordinate system. In this paper, we use the nearest neighbor algorithm to search for corresponding features.

(1) Virtual feature correspondence

Theoretically, the distance from the center of the cross section of the tree stem to the nearest point on the surface of the tree stem is approximately equal to the radius of the cross section, so the point-to-point distance can easily establish a more accurate relationship between the MLS point cloud and the reference. If a distance between a virtual feature and its nearest point in the reference data is approximately equal to the corresponding radius of the virtual feature, then we set the virtual feature point as a keypoint for motion estimation and regard its nearest point in the reference data as its corresponding feature. Let $\tilde{X}_{(V_n,i)}^W$ be a keypoint ($\tilde{X}_{(V_n,i)}^W \in \tilde{V}_n^W$) and $\tilde{X}_{(\Gamma,j)}$ be the corresponding point ($\tilde{X}_{(\Gamma,j)} \in \Gamma_{TLS}$), then the point-to-point distance $d_{(V_n,i)}$ can be computed by

$$d_{(V_n,i)} = \left|\tilde{X}_{(V_n,i)}^W - \tilde{X}_{(\Gamma,j)}\right| \tag{1}$$

for each virtual keypoint, when $d_{(V_n,i)}$ approximates the corresponding radius, the relationship between the keypoint and the corresponding point will be more accurate.

(2) Real feature correspondence

The point-to-plane metric is usually solved using standard nonlinear least squares methods, and the error metric converges much faster. Therefore, in this paper, the planar patch is found to be the corresponding feature of a real feature. If a real feature has three nearest points in the reference data, which are within a certain neighborhood of the real feature point and are not on the same line, then a planar patch consisting of the three points is regarded as a corresponding feature of the real feature, and the real feature point will be used as a keypoint for estimating motion in the MLS system. Let $\tilde{X}_{(R_n,i)}^{W}$ be a keypoint in $\tilde{R}_n^W$ ($\tilde{X}_{(R_n,i)}^{W} \in \tilde{R}_n^W$), and let the corresponding plane be set to $\{\tilde{X}_{(\Gamma,a)}, \tilde{X}_{(\Gamma,b)}, \tilde{X}_{(\Gamma,c)}\} \subset \Gamma_{TLS}$. The distance $d_{(R_n,i)}$ between point and plane can be computed by

$$d_{(R_n,i)} = \frac{\left|\overrightarrow{X_R X_{(\Gamma,a)}} \cdot \vec{n}\right|}{|\vec{n}|} = \frac{\left|\left(\tilde{X}_{(R_n,i)}^{W} - \tilde{X}_{(\Gamma,a)}\right) \cdot \left(\left(\tilde{X}_{(\Gamma,a)} - \tilde{X}_{(\Gamma,b)}\right) \times \left(\tilde{X}_{(\Gamma,a)} - \tilde{X}_{(\Gamma,c)}\right)\right)\right|}{\left|\left(\tilde{X}_{(\Gamma,a)} - \tilde{X}_{(\Gamma,b)}\right) \times \left(\tilde{X}_{(\Gamma,a)} - \tilde{X}_{(\Gamma,c)}\right)\right|} \tag{2}$$

where $\vec{n}$ is the normal vector of the plane. For each real keypoint, when the $d_{(R_n,i)}$ is smaller and tends towards 0, the relationship of the corresponding pair will be more stable.

3.3.3 Motion estimation

This step is to achieve registration using the corresponding pairs built by the virtual features and the real features. Let T_n^W be the transformation vector between the MLS point cloud $\tilde{M}_n^W$ and the reference Γ_{TLS}. T_n^W contains rigid motion in 6 degree of freedom (DOF); i.e.,

$$T_n^W = [\omega, \varphi, \kappa, t_x, t_y, t_z]$$

Where ω, φ and κ are rotations around the x-, y-, z-axes of $\{W\}$, respectively, following the right-hand rule. t_x, t_y and t_z are translations of $\{W\}$ along the x-, y- and z-axes, respectively. Let us assume that $\tilde{X}_{(n,i)}^{W}$ are the feature points from $\tilde{V}_n^W$ and $\tilde{R}_n^W$, where the features are extracted from the MLS point cloud, and $X_{(n,i)}^{W}$ are the transformation results of $\tilde{X}_{(n,i)}^{W}$. To estimate accurate motion of the MLS system, a rigid transformation relationship between $X_{(n,i)}^{W}$ and $\tilde{X}_{(n,i)}^{W}$ can be established:

$$X_{(n,i)}^{W} = R\tilde{X}_{(n,i)}^{W} + T_n^W(1:3) \tag{3}$$

where R is the rotation matrix ($R \in R^{3\times3}$). In this paper, we consider the y-axis as the principal axis and calculate R by rotating around the y-x-z axis.

$$R = R_y(\varphi)R_x(\omega)R_z(\kappa) = \begin{bmatrix} cos\varphi cos\kappa - sin\varphi sin\omega sin\kappa & -cos\varphi sin\kappa - sin\varphi sin\omega cos\kappa & -sin\varphi cos\omega \\ cos\omega sin\kappa & cos\omega cos\kappa & -sin\omega \\ sin\varphi cos\kappa + cos\varphi sin\omega sin\kappa & -sin\varphi sin\kappa + cos\varphi sin\omega cos\kappa & cos\varphi cos\omega \end{bmatrix}$$

From Eq. (1), we can derive a geometric relationship between each virtual keypoint in the MLS data and the corresponding point in the reference:

$$f_V\left(\tilde{X}_{(n,i)}^{W}\right) = d_V - r_{(V_n,i)}, \tilde{X}_{(n,i)}^{W} \in \tilde{V}_n^W \tag{4}$$

Similarly, from Eq. (2), we can derive a geometric relationship between each real keypoint in the MLS data and the corresponding planar patch in the reference:

$$f_R\left(\tilde{X}_{(n,i)}^{W}\right) = d_R, \tilde{X}_{(n,i)}^{W} \in \tilde{R}_n^W \tag{5}$$

Combining Eq. (4) and Eq. (5), a nonlinear function about T_n^W can be established:

$$f(T_n^W) = d = \sum f_V\left(\tilde{X}_{(n,i)}^{W}\right) + \sum f_R\left(\tilde{X}_{(n,i)}^{W}\right) \to 0 \tag{6}$$

where each row of f corresponds to a keypoint and d represents distance between the keypoint and its corresponding

feature. Finally, we can solve Eq. (6) through nonlinear iterations by minimizing the error e toward zero with the Levenberg-Marquardt (L-M) method:

$$e = \underset{e}{argmin}\frac{1}{2}\sum_{i=1}^{N}\|d_i - 0\|^2 = \underset{e}{argmin}\frac{1}{2}f(T_n^W)^T f(T_n^W) \tag{7}$$

First, we linearize Eq. (7) with the first-order approximation of a Taylor expansion:

$$f(T_n^W) = f\left(\hat{T}_n^W + \Delta T\right) = f\left(\hat{T}_n^W\right) + J\Delta T \tag{8}$$

where $\hat{T}_n^W$ is the initial motion in 6-DOF and ΔT is the correction of the initial motion. In this paper, 6-DOF T_n^W, i.e., the rotations $(\omega, \varphi, \kappa)$ and the translations (t_x, t_y, t_z), are regarded as the unknowns, and J is the Jacobian matrix of $f(\cdot)$ and can be calculated by combining Eq. (3) and Eq. (6):

$$J = \begin{bmatrix} \frac{\partial f}{\partial \omega} & \frac{\partial f}{\partial \varphi} & \frac{\partial f}{\partial \kappa} & \frac{\partial f}{\partial t_x} & \frac{\partial f}{\partial t_y} & \frac{\partial f}{\partial t_z} \end{bmatrix} \tag{9}$$

By combining Eq. (3) to Eq. (6), we derive every element of matrix J. Taking a virtual feature point (x, y, z) as example to describe the derivation of ω,

$$\frac{\partial f}{\partial \omega} = \frac{\partial f_V}{\partial X_{(n,i)}^W}\cdot\frac{\partial X_{(n,i)}^W}{\partial \omega} = \frac{\partial f_V}{\partial x}\cdot\frac{\partial x}{\partial \omega} + \frac{\partial f_V}{\partial y}\cdot\frac{\partial y}{\partial \omega} + \frac{\partial f_V}{\partial z}\cdot\frac{\partial z}{\partial \omega} =$$
$$\frac{x - x_\Gamma}{d_v}\cdot\left(\frac{\partial R_{11}}{\partial \omega}\cdot x + \frac{\partial R_{12}}{\partial \omega}\cdot y + \frac{\partial R_{13}}{\partial \omega}\cdot z\right) + \frac{y - y_\Gamma}{d_v}\cdot\left(\frac{\partial R_{21}}{\partial \omega}\cdot x + \frac{\partial R_{22}}{\partial \omega}\cdot y + \frac{\partial R_{23}}{\partial \omega}\cdot z\right) +$$
$$\frac{z - z_\Gamma}{d_v}\cdot\left(\frac{\partial R_{31}}{\partial \omega}\cdot x + \frac{\partial R_{32}}{\partial \omega}\cdot y + \frac{\partial R_{33}}{\partial \omega}\cdot z\right)$$

where $(x_\Gamma, y_\Gamma, z_\Gamma)$ is the closest neighboring point of (x, y, z) in single-scan TLS point cloud, d_v is the distance between (x, y, z) and $(x_\Gamma, y_\Gamma, z_\Gamma)$, and R_{ij} represents the element in rotation matrix R. Similarly, we can derive all the other elements of matrix J. In addition, according to the virtual and real features, we can construct the Jacobian matrix J with size of $M \times 6$, where M denotes the sum of the number of the virtual features and the number of the real features. By deriving Eq. (7) with 0, then combining Eq. (8) and Eq. (9), the correction ΔT can be solved by

$$\Delta T = (J^T J + \lambda I)^{-1} J^T d \tag{10}$$

where λ is the damping factor determined by the L-M method. Then, fine motion can be calculated by

$$T_n^W = \hat{T}_n^W + \Delta T \tag{11}$$

where the MLS point cloud can be transformed into the world coordinate system based on T_n^W.

3.3 Global optimization

Global optimization is to eliminate the cumulative error and transform all point clouds into a global coordinate system (Shao et al., 2019). The challenge of global optimization is solving the spatial inconsistency problem (Liang et al., 2018). Therefore, we adopt a method based on global map that does not consider the loop closure and the adjustment of all of the data to address the global optimization of SLAM. In this paper, the single-scan TLS point cloud is used as a reference, and a global map combining the reference and incremental MLS point clouds provides a global constraint for forest mapping. The detailed schematic is shown as Fig. 5.

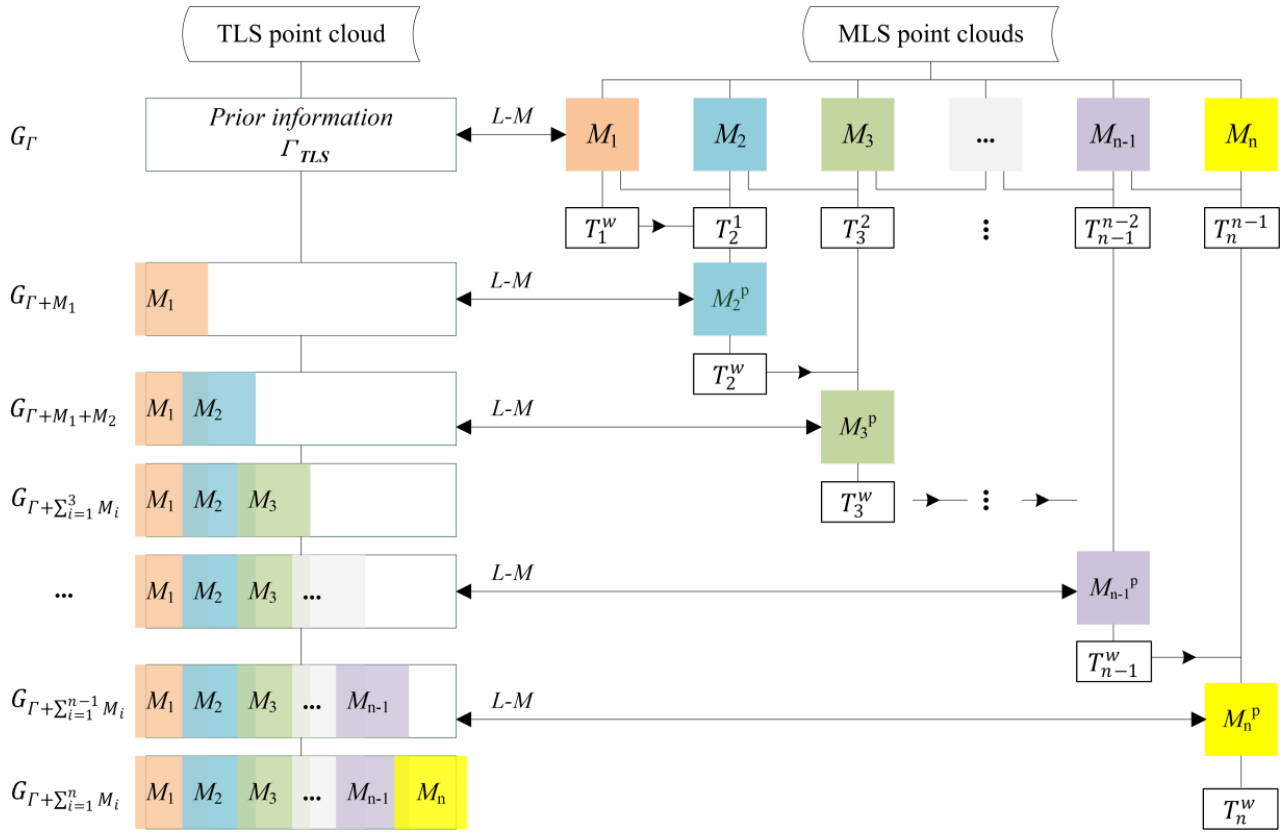

Fig. 5. Schematic of global optimization. $\{M_1, M_2, M_3 \ldots M_n\}$ with different colors represent the MLS point clouds at different time. T_i^W represents the motion of MLS data at the time of sweep *i*, and M_i^p represents an initial transformed MLS point cloud. $G_{\Gamma+\sum_{i=1}^{n} M_i}$ represents the global cumulative map.

Let a world coordinate system $\{W\}$ be the global coordinate system and M_k (k=1, 2, 3 … n-1, n) represents an MLS point cloud at the time of sweep k, where forest mapping starts from point cloud M_1. For M_1, we set prior information Γ_{TLS} as the reference and optimize the transformed M_1 using the L-M method. Then, we can obtain the motion T_1^W of MLS data at the time of sweep 1 and transform M_1 into a global coordinate system. Simultaneously, we build the global map $G_{\Gamma+M_1}$ by combining Γ_{TLS} and M_1 and reset $G_{\Gamma+M_1}$ as the global constraint.

For an MLS point cloud M_2 at the time of sweep 2, we calculate the transformation T_2^1 between M_1 and M_2 using 3D-NDT; then, an initial transformation $\hat{T}_2^W$ between M_2 and the global map $G_{\Gamma+M_1}$ can be calculated based on T_1^W and T_2^1. Furthermore, an initial transformed point cloud M_2^p from the local coordinate system of M_2 to the global coordinate system $\{W\}$ can be obtained based on $\hat{T}_2^W$. Because of the propagation of error, we optimize the initial transformation $\hat{T}_2^W$ and the transformed point cloud M_2^p based on the global map $G_{\Gamma+M_1}$ using the L-M method. In the process, the corresponding points of virtual keypoints and the corresponding patches of real keypoints are extracted from the global map $G_{\Gamma+M_1}$. According to the L-M method, we can obtain an optimized transformation T_2^W and a point cloud M_2^W. Simultaneously, we rebuild a new global map $G_{\Gamma+M_1+M_2}$ by combining $G_{\Gamma+M_1}$ and M_2^W. Similar to the MLS point cloud M_2, we can estimate the motion T_i^W of the subsequent MLS point clouds and transform each MLS point cloud M_i into a global map and rebuild a new cumulative global map $G_{\Gamma+\sum_{i=1}^{n} M_i}$. We locate each MLS point cloud in the global coordinate system $\{W\}$ and simultaneously map the environment by combining the MLS data and the single-scan TLS data.

In practice, some MLS point clouds affected by motion distortion and measurement error reduce the accuracy of forest mapping. Therefore, we detect the key MLS point cloud by judging the relationship between the virtual keypoints and their corresponding points (Eq. (1) and (4)). If the difference between the points in the corresponding

pair is less than the set threshold, we add the current point cloud to the global map.

4. Results and discussion

4.1 Study area and data collection

The study area, located in Saihanba National Forest Park in Hebei Province in northern China, is dominated by coniferous trees. The study area includes dozens of square sample plots of size 25 m ~ 30 m, and the tree species is larch. For this study, we selected data from three test areas: Plot A ~ Plot C (Fig. 6). In Plot A, we acquired two sets of point cloud data at different periods, Plot A1 and Plot A2. In the three plots, the stem density is approximately 625 stems/ha, the mean height is approximately 19.0 m. In addition, the maximum diameter at breast height (DBH) is approximately 0.33 m, the minimum DBH is approximately 0.2 m, the mean DBH is approximately 0.27 m, and the standard deviation of DBH is approximately 0.03 m.

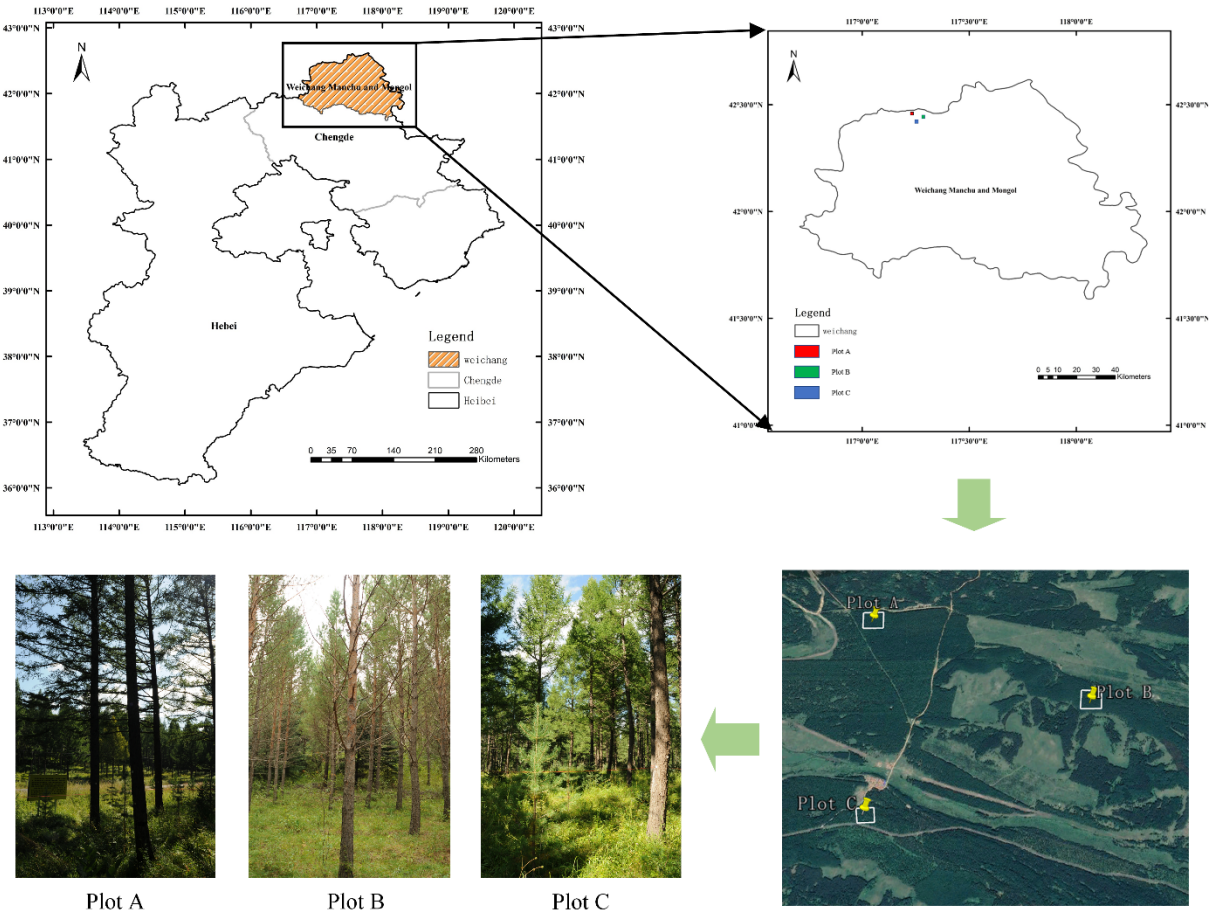

Fig. 6. Study area.

The MLS data were captured using the Velodyne VLP-16 laser scanning system. Its angular resolution was 2° in the vertical direction, and the scan frequency was set to 10 Hz. The MLS data were captured by cross-moving around the forest plots, and we obtained 1918 MLS point clouds in plot A and 1395 point clouds in plot B. The TLS data were captured using the Riegl VZ-1000 laser scanning system, and the scan angular resolution is 0.03° in both horizontal and vertical directions. The TLS system was placed in the middle of the forest plot to acquire point clouds with a full field-of-view scan. In addition, the multi-scan TLS mode was also used to verify and compare methods. Table 1 gives the related parameters of the two scanners.

Table 1

Parameters of the used laser scanners.

Scanner	MLS (Velodyne VLP-16)	TLS (Riegl VZ-1000)
Channels	16	1
Range (max.)	~100 m	~1,400 m
Measurement rate (max.)	600,000 points/sec	122,000 points/sec
Field of view (horizontal × vertical)	360° × 30° (+15° / -15°)	360° × 100° (+60° / -40°)
Measurement precision	±3 cm	±0.5 cm

4.2 Evaluation of feature extraction

Due to the universality of the real features, we just evaluated the effectiveness of the proposed virtual features in this paper. The virtual feature is represented by the center of the tree stem cross section, so we used the radius that correspond to the center to evaluate the virtual feature. Specifically, the deviation between the radius from the MLS data and its corresponding radius from the single-scan TLS data was calculated and used for evaluation of the extracted virtual features. Fig. 7 shows the evaluation results from one frame MLS point cloud.

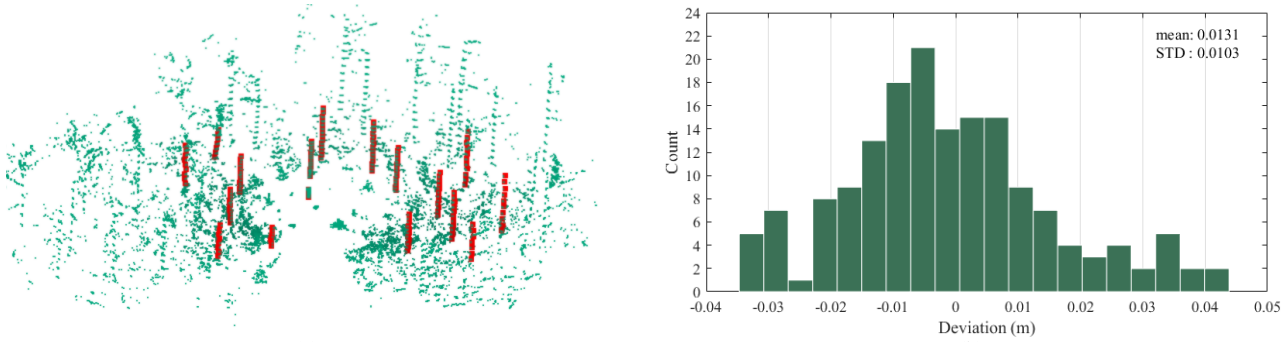

Fig. 7. Extraction of the virtual features. (a) The result of virtual features extraction (red points are the extracted virtual features, and green points represent raw MLS point cloud); (b) the distribution of the radius deviations, x-axis represents the deviations and y-axis represents count of virtual features in different deviation ranges.

To ensure reliability and correctness of the virtual features, strong constraints were used for feature extraction. For example, virtual feature point are discarded if they have a radius that is significantly different from the other feature points on the same tree. Therefore, although this method was unable to detect all trees in the MLS data, the virtual features from the remarkable trees with dense points could be correctly extracted (Fig. 7 (a)). Fig. 7 (b) show that the radius deviations of the virtual features is small, e.g., the radius deviations of almost all virtual features stays within -0.03 m ~ 0.03 m and the virtual feature points deviations stays within -0.02 m ~ 0.02 m in most cases. In addition, the mean absolute deviation and the standard absolute deviation were approximately 0.01 m, which indicated the reliability of the virtual feature points. However, some factors, such as the curvature of the trunk and number of the fitted points, could lead to relatively large deviations. Because the radius deviations of most virtual feature points were small, the results also suggested the reliability of virtual features for accurate feature matching.

4.3 Evaluation of corresponding pairs

In this paper, the corresponding pairs were composed of the feature points from each frame MLS point cloud and their nearest neighbor points from single-scan TLS point cloud, of which the distance deviation between the pairs was regarded as constraint for motion estimation of the MLS system. Therefore, we used Eq. (1) and Eq. (2) to quantitatively evaluate the performance of the corresponding pairs, of which the deviation between the value of Eq. (1) and the corresponding radius and the value of Eq. (2) were regarded as evaluation indices for evaluating the

corresponding pairs of the real features and the virtual features, respectively (Fig. 8).

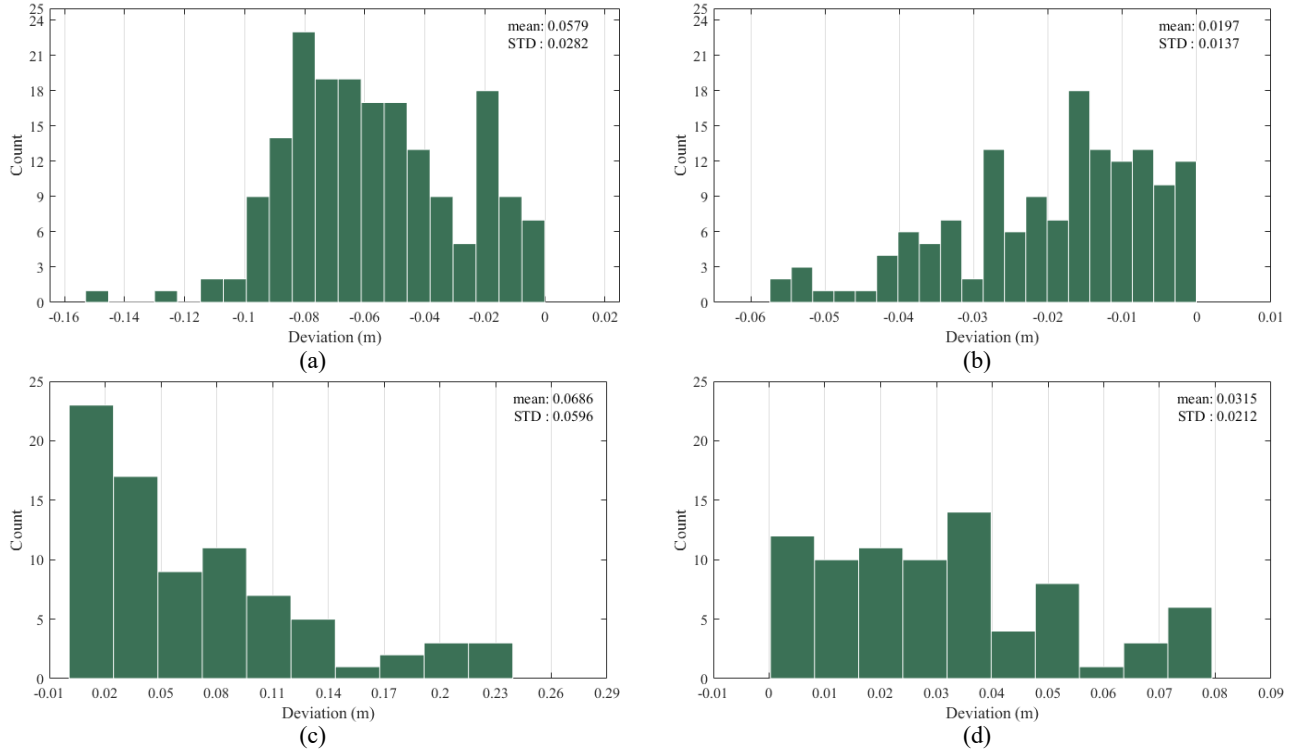

Fig. 8. Evaluation of the corresponding pairs, x-axis denotes the deviations and y-axis denotes count of features in different deviation ranges. (a) and (b) represent relation between the virtual features in the MLS data and their corresponding features in the single-TLS data before and after nonlinear optimization, respectively. (c) and (d) represent the distance deviations between the real features in the MLS data and their corresponding features in the single-TLS data before and after nonlinear optimization, respectively.

For virtual features, because the tree stem cross section is not exactly round, the distance between the center of the cross section to its closest point on the surface of the trunk is usually less than the corresponding radius, and the deviation between the distance and the radius is less than 0 (see Fig. 8 (a) and (b)). As the number of iterations during the optimization increases, the corresponding pairs will change. In generally, the deviations are large before iteration begins. For example, the deviations of most virtual features are within -0.1 m ~ -0.03 m, and the mean and standard absolute deviations are approximately 0.058 m and 0.028 m, respectively (see Fig. 8 (a)), which indicate inaccurate scan matching in the horizontal direction. From Fig. 8 (c), the deviations of most real features are within 0.0 m ~ 0.14 m, the mean and standard absolute deviations are approximately 0.068 m and 0.059 m, respectively. Apparently, with initial pose of the MLS system, the corresponding pairs that derived from the MLS data and the single-scan TLS data are difficult to achieve accurate motion estimation. Therefore, nonlinear optimization is used to update the corresponding pairs. In theory, if the accurate corresponding pairs can be generated at the end of the iterations, the deviation values will be small and tend to zero. For example, the deviations of most virtual features are within -0.03 m ~ 0.0 m, and the mean and standard absolute deviations dropped to approximately 0.02 m and 0.014 m, respectively (see Fig. 8 (b)), of which several factors, such as the inaccurate features and the non-circular cross section of tree stem, led large deviations in the results. For the real features, most deviations are within 0.0 m ~ 0.05 m, the mean and standard absolute deviations dropped to approximately 0.032 m and 0.021 m, respectively (in Fig. 8 (d)). In addition, because some inaccurate corresponding pairs were discarded in the process of nonlinear optimization, the total number of features decreased. In general, the evaluation results showed certain reliability of the corresponding pairs, especially the virtual feature points and their corresponding points, which also indicated a possibility for achieving accurate motion estimation of the MLS system.

4.4 Forest mapping and positioning accuracy

In the proposed method, two results can be obtained: localization and mapping. The localization is represented by the trajectory of the MLS system, and the mapping is represented by the reconstruction of the forest plots. To evaluate the robustness of the proposed method in forests, we tested two forest plots in which the movements of the MLS system were along with different trajectories (see Fig. 9).

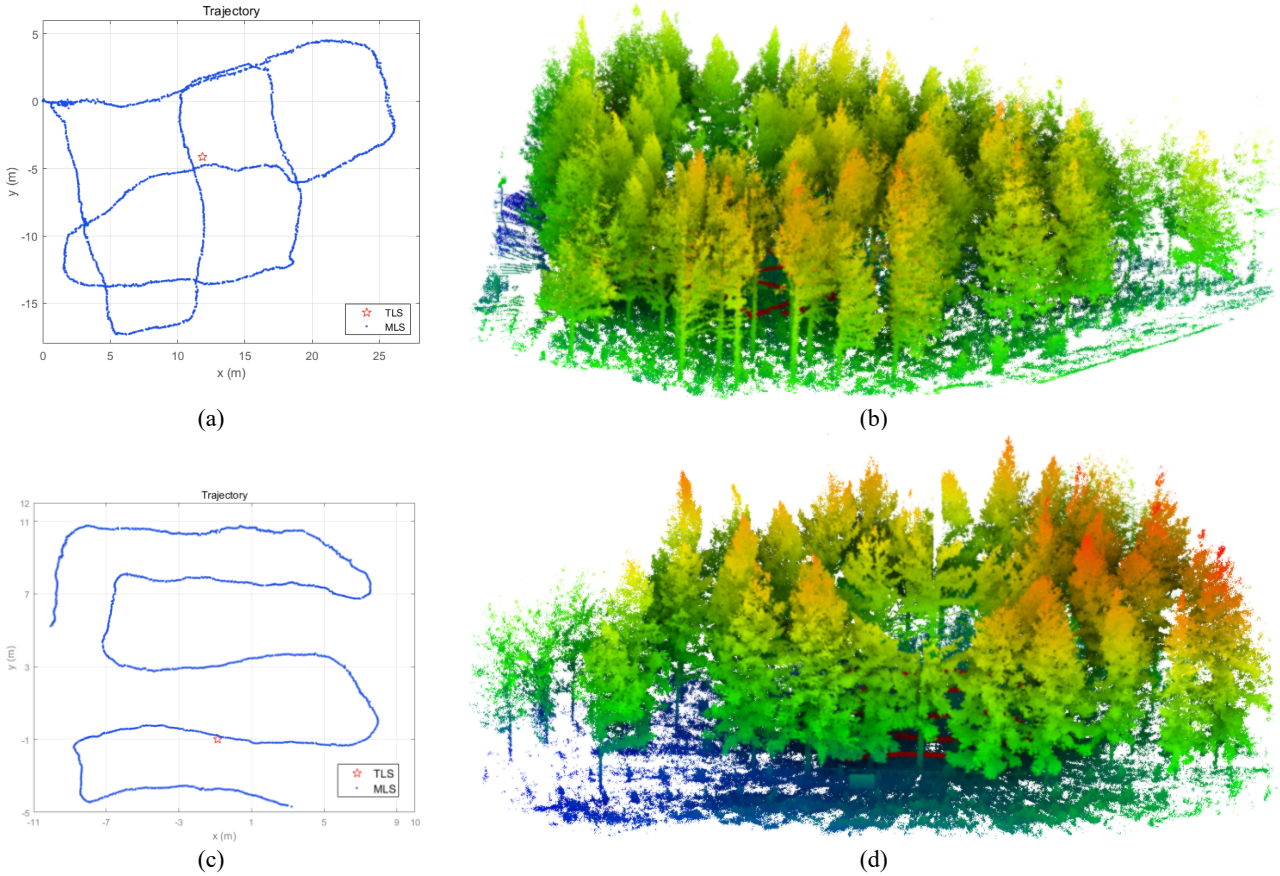

Fig. 9. Forest mapping results. (a) and (b) represent mapping in plot A, (c) and (d) represent mapping in plot B. (a) and (c) represent the trajectories of MLS system in the two plots (blue points are the positions of the MLS system and red stars represent scan positions of single-scan TLS). (b) and (d) show the reconstruction results of the two forest plots.

The results in Fig. 9 (a) and (c) are coincident with the practical movements of the MLS system. Fig. 9 (b) and (d) show that the forest plots can be reconstructed, and the distribution and shape of individual trees reconstructed by the proposed method are clear and identifiable. In the reference data, the locations of tree stems were available for evaluation of planimetric accuracy, so to quantitatively evaluate the performance of the proposed method, the locations of stems obtained from the proposed method were compared to those from the TLS data. The accuracy results of the stem position are summarized in Table 2.

Table 2

Stem position accuracy. 'Plot' column represents the plot index. 'Trees' column gives the number N_T of the detected trees in each plot. Stem position deviation is calculated planimetric distance between the detected tree and its reference.

Plots	Trees	Stem position deviations		
	N_T	Mean (m)	STD (m)	Max (m)
Plot A1	22	0.0126	0.0057	0.0233
Plot A2	16	0.0147	0.0056	0.0248
Plot B				
Plot C				

In plot A1 and plot A2, 22 trees and 16 trees were used to evaluate the accuracy of the proposed method, respectively. The means of stem position deviations varied between 0.012 m and 0.015 m. The standard deviations were at the millimeter level, which indicated accurate forest plots mapping results. The results in Table 2 reveal the small stem position deviation values. Combining the results in Fig. 9, the location and orientation of the optimized data do not drift from their correct values during global optimization, e.g., the trajectory of the MLS system can be closed without loop-closure detection in plot A (see Fig. 9 (a)), and the open trajectory of the MLS system in plot B can still be accurately recovered by the proposed method (see Fig. 9 (c)). Therefore, the reference, i.e., single-scan TLS data, can provide an effective global consistency constraint for MLS-based forest mapping, of which those virtual features retain the absolute accuracies of the tree stem locations in the horizontal direction.

In addition to evaluation of planimetric accuracy, we selected some remarkable feature points from ground and branches and compared with their corresponding points in TLS data to reflect the mapping accuracy in the vertical direction. The tree branch position deviations in the vertical direction were calculated for evaluation of mapping accuracy in this paper. In practice, 15 feature points on the branches were evenly selected from each of the three plots for evaluate the vertical accuracy. The accuracy results are shown in Table 3.

Table 3

Vertical accuracy. 'Plot' column represents plot index. 'Points' column gives the number N_P of the selected sample points on branches or ground of each plot. The deviation is calculated vertical distance between the sample point and its reference in TLS.

Plots	Points	Vertical deviations		
	N_P	Mean (m)	STD (m)	Max (m)
Plot A1	15	0.0203	0.0117	0.0426
Plot A2	15	0.0192	0.0135	0.0438
Plot B				
Plot C				

From Table 3, the deviations were at the centimeter level in the test plots, of which the mean deviations were approximately 0.02 m, the standard deviations were approximately 0.01 m, and the maximum deviations were less than 0.05 m. Because the constraints from the ground and canopy points, especially the ground, the NDT algorithm could maintain the mapping accuracy in the vertical direction; meanwhile, the real features further optimized the vertical accuracy using even-distributed points in forest, and the proposed optimization framework provided certain global consistency constraint for the MLS-based forest plots mapping. In forest measurements, the requirement of the vertical accuracy is generally lower than that in horizontal accuracy (e.g., tree height measurement), which is at the centimeter or decimeter level. Therefore, the results in Table 3 indicated highly accurate mapping results in the vertical direction. Overall, the results from Fig. 9, Table 2, and Table 3, suggested a certain reliability and robustness of the proposed method.

4.5 Data completeness and performance

The completeness of the structural information is an important basis on which to the select a data acquisition method. The paper combined the single-scan TLS and MLS data to reconstruct the forest plots so that the MLS data could offer compensation for the omission of single-scan TLS data. Therefore, to assess the effectiveness and advantages, we analyzed and compared the data completeness on the plot scale by the proposed method with the single-scan TLS data. The results in plot A are shown in Fig. 10.

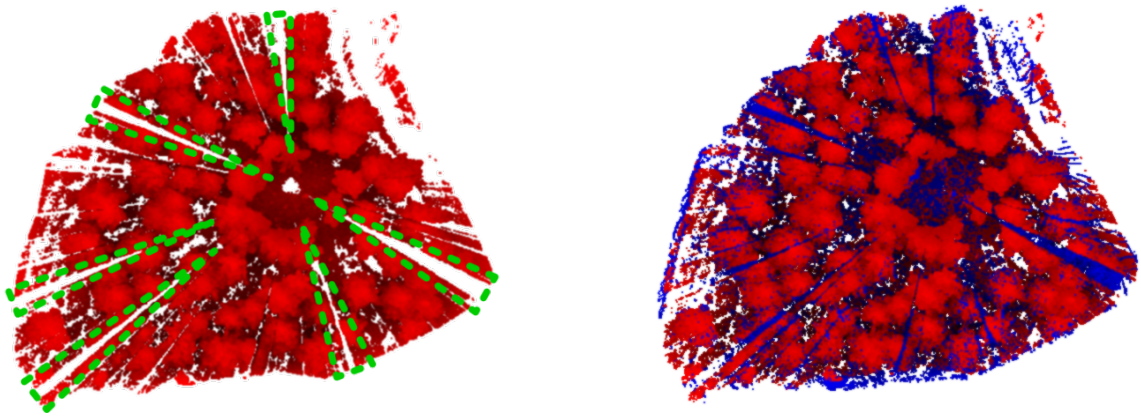

(a) (b)

Fig. 10. Comparison between the single-scan TLS point cloud and the result of the proposed method. (a) represents the single-scan TLS point cloud (red points), green triangles show the omitted regions. (b) represents the mapping result of the proposed method (red points are the single-scan TLS point cloud and blue points are the MLS data).

As shown in Fig. 10 (a), due to the occlusion effects from the other objects, there are some regions that cannot be scanned by the single-scan TLS at the forest plot scale, such as the sector regions labeled by the green triangles. According to the proposed method, these omitted regions can be filled by the MLS point clouds (Fig. 10 (b)). Thus, the proposed method can obtain more complete structural information of the forest. In addition, the ground-based LiDAR systems are mainly used for data acquisition below the canopy, of which the tree stem is one of the significant tree-level attributes that is being widely studied. Therefore, to evaluate the advantages of the proposed method, we compared it with the single-scan TLS method and multi-scan TLS method from the completeness of individual tree stem data in plot A1. Fig. 11 shows a comparison of the three data acquisition methods.

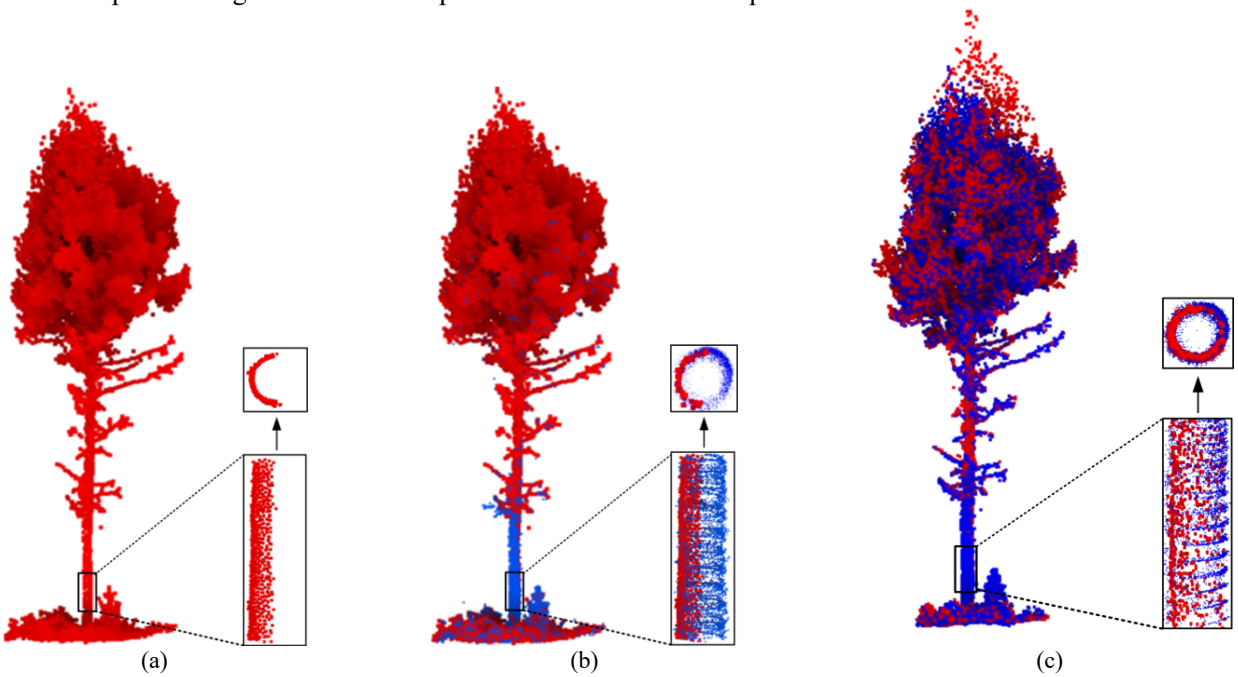

(a) (b) (c)

Fig. 11. Comparison of individual trees mapping. (a) Tree mapping by the single-scan mode. (b) Comparison between the single-scan TLS mode (red points) and the proposed method (blue points). (c) Comparison between the multi-scan TLS mode (red points) and the proposed method (blue points).

From the side view and the cross section of the tree stem in Fig. 11 (a), only one side of the tree stem can be scanned by the single-scan TLS method because the laser cannot penetrate the tree stem. Fig. 11 (b) shows that the omission of tree stem data caused by one scan (see Fig. 11 (a)) can be compensated for by the MLS data of the

proposed method. Fig. 11 (c) shows that the proposed method and the multi-scan TLS method acquired a complete stem structure. Nevertheless, the structural information above the canopy acquired by the multi-scan TLS method is more complete than that of the proposed method. Furthermore, due to the limitation of field of view, a single MLS scanner can only achieve stems mapping using the proposed approach, and the canopy structural information is generally limited. Consequently, the individual tree attributes related to tree height are difficult to estimate accurately. On the contrary, the attributes related to the DBH can be obtain because the completeness of the stem points. Therefore, to assess the performance of the MLS data, we evaluate the DBH and the stem curve.

The DBH is an important structural parameter in forestry inventories and can be used to analyze tree growth. Therefore, we calculate the DBH based on the point cloud from plot A and compare the result with that from the single-scan TLS. The DBH of individual trees is determined by extracting a cross section of point cloud that falls between 1.2 m and 1.4 m above the ground level. Therefore, we first filtered the ground and non-ground points (Zhang et al., 2016b) and extracted points that represented the tree stem hull at breast height from the non-ground points and then use the least squares method to fit a circle to these points. To evaluate the accuracy of the fitted DBH by the proposed method and single-scan TLS, the DBH fitted by the precise multi-scan TLS data was used as the reference in this paper. In total, 22 trees were detected for the measurement of DBH values in plot A. The accuracy of the DBH values is assessed by treating the reference as a variable that is dependent upon the fitted measurement and running a simple linear regression analysis to determine the correlation coefficient (R^2) for the two related datasets (see Fig. 12).

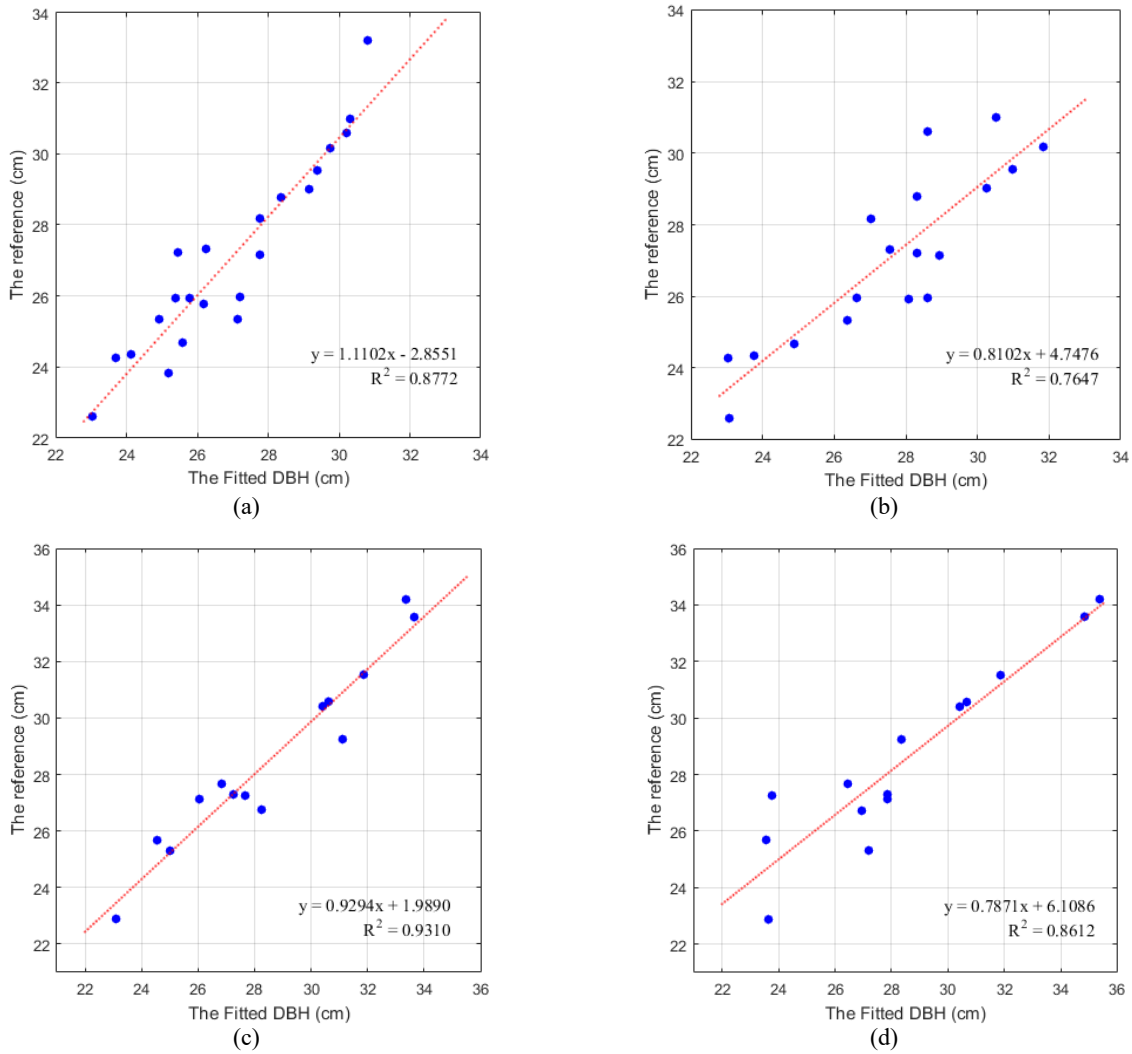

Fig. 12. Scatter plots of the DBH values, (a) and (b) are derived from the data of Plot A1, and (c) and (d) are derived from the data of Plot A2. Y-axis represents the reference of DBH values, and x-axis in (a) and (c) represents the DBH fitted by the proposed method, x-axis in (b) and (d) represents the DBH fitted by the single-scan TLS data (excluding extreme outlier).

In the data of Plot A1 and Plot A2, the fitted DBH of 22 trees and 14 trees are considered in a statistical analysis, respectively. The linear regression analysis reveals that the correlation coefficient R^2 values between the fitted DBH measured from data via the proposed method and the fitted DBH from the multi-scan TLS data are 0.8772 and 0.9310, respectively (Fig. 12 (a) and (c)). The root mean square error (RMSE) is 0.96 cm, and the mean absolute error (MAE) is 0.75 cm in Plot A1. In Plot A2, the RMSE and MAE values are approximately 0.84 cm and 0.62 cm, respectively. For the single-scan TLS data in Plot A1, the R^2 for the DBH is 0.7152. The RMSE between the fitted DBH values and the field-measured DBH values is 1.92 cm, and the MAE is 1.57 cm. When we remove the individual trees with fitted DBH values that are more than +/- 10% of the field-measured value, 4 trees were removed from the plot, which resulted in a new correlation coefficient (R^2) of 0.7647 in Fig. 12 (b), and the RMSE value and MAE value decreased to 1.33 cm and 1.14 cm, respectively. For the single-scan TLS data in Plot A2, the R^2 value is 0.8612, and the RMSE value and MAR value are approximately 1.39 cm and 1.06 cm, respectively (see Fig. 12 (d)). As a result, in addition to data completeness, the proposed method can obtain more accurate DBH values than the results from the single-scan TLS method.

In forest measurements, the stem curve is usually used to describe the shape of tree stem and consists of stem diameters from specific tree height. In order to evaluate the accuracy of the extracted stem curve, we compared the diameters from the MLS data to the reference diameters from the multi-scan TLS data, of which the corresponding diameters were at the same heights. The accuracy of the stem curves that extracted from the data of Plot A1 and Plot A2, including mean absolute error (MAE), root mean square error (RMSE), and the maximum deviation, are summarized in Table 4.

Table 4

The accuracy of the stem curve. 'Plot' column represents the plot index. 'Stems' column gives the number N_T of the detected stems in each data set. Stem curve is calculated by averaging the diameters at different heights.

Plots	Stems	Stem curve deviations		
	N_T	MAE (m)	RMSE (m)	Max (m)
Plot A1	10	0.0204	0.0096	0.0464
Plot A2	10	0.0234	0.0077	0.0408

In Table 4, 10 trees from each of the two sets of data were selected to evaluate the stem curves. The MAE values were at the centimeter level, approximately 0.02 m, and the RSME values were approximately 0.01 m. The results indicated the overall correctness of the stem curve could reach 90% in the test plot. In addition, the maximum deviations were 0.0464 m and 0.0408 m, respectively, of which their common characteristic was that the completeness of their corresponding stem data was low. On the contrary, the stem curve deviation was generally small when the stem data were complete. Although the accuracy of the stem curve suggested certain effectiveness of the data from the proposed method, complete stem point cloud was commonly required for achieving accurate calculation of the stem curve.

4.6 Comparison of data acquisition methods

Compared to the TLS system, the major of advantage the MLS system is the rapid acquisition of point cloud. In addition, one of the purposes of this paper is to supplement the single-scan TLS point cloud with the MLS data, of which the tree stem is one of significant tree attributes that is supplemented. Therefore, to assess advancement of the proposed method, we compared it with the single-scan TLS method and multi-scan TLS method from the time of field measurement and the completeness of tree stem data in plot A (Table 5).

Table 5

The completeness of individual tree stem data and the time of the field measurement in plot A. "Criteria" column lists two evaluation criteria, "%" represents point cloud coverage rate.

Criteria	Data acquisition methods		
	Single-scan TLS	Multi-scan TLS	The proposed method
Time of the field measurement (min)	≈ **20 min**	≈ 210 min	≈ 25 min
Completeness of tree stem data (%)	< 50 %	≈ **100 %**	≈ **100 %**

At the time of the field measurement, the single-scan method needs the least amount time of the three methods. To ensure an adequate precision and detection rate, we took approximately 20 minutes for the field measurement: selection of scan position and setup of scanner took 5-10 minutes, and a full field-of-view scan in fine-scan mode took approximately 10 minutes. In the proposed method, single-scan TLS and MLS were combined for data acquisition. In addition to single-scan TLS, the MLS system took approximately 5 minutes to acquire point clouds in a forest plot, included planning trajectory and scanning. In total, the proposed method took approximately 25 minutes for plot A. In practice, the TLS system of the proposed method can be directly placed at the middle of the forest plot and acquires point cloud with a coarse-scan mode, and we do not consider the detection rate and the precision of trees in the placement of the TLS system, which only take 5-10 minutes to set up and scan the plot. In theory, therefore, we only need approximately 15 minutes to scan plot A. On the other hand, the multi-scan TLS method used five scan positions to scan plot A with fine-scan mode and placed some reflective targets in the plot for point cloud registration. As a result, the method took approximately 210 minutes to field-measure one plot. Therefore, single-scan TLS and the proposed method are more efficient (see Table 5).

To evaluate the completeness of the tree stem data, the single-scan TLS method only scanned one side of the tree stem, which led to a low detection rate because of occlusion effects. The coverage rate of tree stems was less than 50%. The multi-scan TLS method and the proposed method acquired more complete tree stems from multiple perspectives in the forest plots, and their point cloud coverage rates of the tree stems were approximated 100%. Regardless of the completeness of the detection rate of the stems, the multi-scan TLS method and the proposed method are better than the single-scan TLS method (see Table 5).

In conclusion, according to the evaluation criteria, the three data acquisition methods all have their own advantages. When the amount of time needed for field measurements is of interest, single-scan TLS method and the proposed method are the best choices. If the completeness of the stem is needed, multi-scan TLS and the proposed method have a slight advantage over single-scan TLS. Nevertheless, if the completeness of tree stems and the time needed for field measurements are all considered together, the proposed method may be the best choice.

4.7 Comparison of motion estimation

The point cloud registration error in the forest environment is generally reflected in the fusion of tree stems, so we evaluated the proposed method according to the locations of tree stems. Furthermore, we compared the proposed method with current, popular methods: NDT, the ICP method, and the LOAM method. To assess the performance of these methods, we visualized the cross sections of four tree stems in the low-overlap and high-overlap regions of the two plots. The results are shown in Table 6.

Table 6

Cross sections of four tree stems in registration results by different methods (red points are from TLS point cloud; blue points are from MLS point cloud). Each line represents a tree stem data.

Methods	NDT	LOAM	ICP	The proposed method

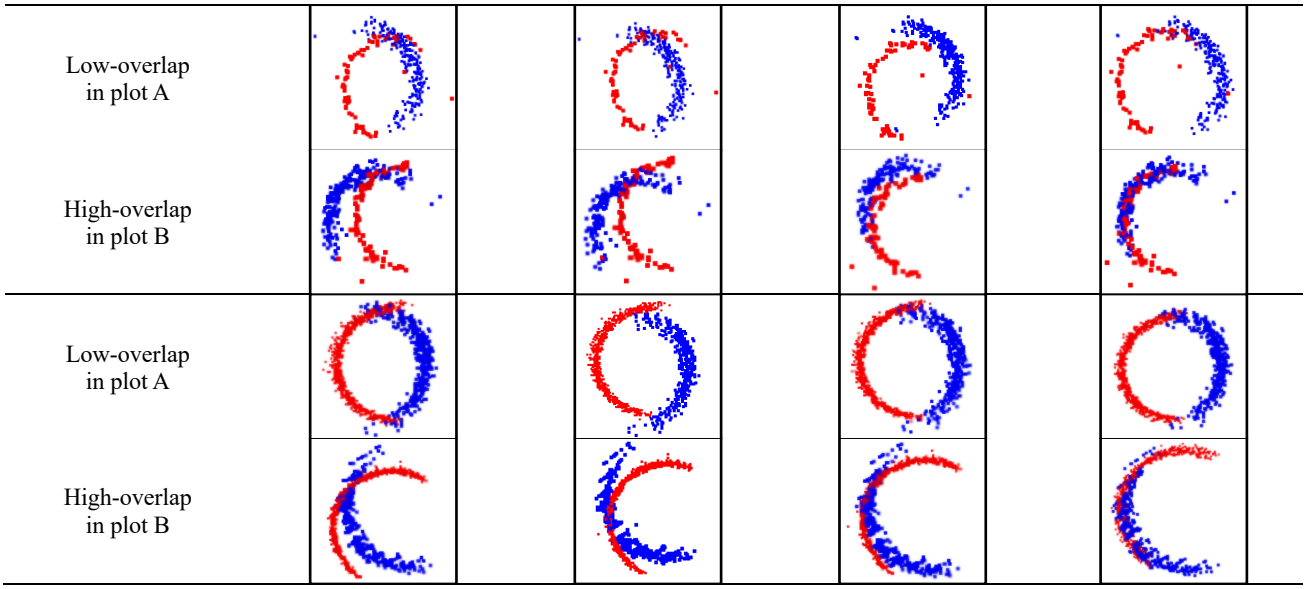

From Table 6, distinct deviations were observed in the results from the NDT, LOAM, and ICP methods. The deviations of the NDT and LOAM methods are similar and more obvious, and the stem points in the MLS data transformed by the two methods intersect with the reference points, especially the stems in the high-overlap region of the two plots. In contrast, the results of the proposed method showed that the cross sections of the tree stems in the low-overlap region are approximately circular, and the tree stems in the MLS point cloud transformed by the proposed method in the high-overlap regions of the two plots also agree with the TLS data. Furthermore, to evaluate the overall accuracy of registration, we detected several easily identifiable tree stems to calculate the stem position deviations and compared the performances of the four methods. The results are summarized in Table 7.

Table 7

Stem position accuracy of different methods.

Plots	Methods	Trees	Stem position deviations		
		N_T	Mean (m)	STD (m)	Max (m)
Plot A1	NDT	11	0.0705	0.0259	0.0995
	LOAM	12	0.0655	0.0272	0.1041
	ICP	13	0.0584	0.0234	0.1021
	The proposed method	11	**0.0129**	**0.0048**	**0.0207**
Plot A2	NDT	10	0.0449	0.0210	0.0798
	LOAM	10	0.0444	0.0171	0.0667
	ICP	11	0.0315	0.0115	0.0549
	The proposed method	10	**0.0076**	**0.0068**	**0.0264**

The results show large deviations in the results from the NDT, LOAM, and ICP methods. In practice, the three methods consider the points on different sides of one tree stem to be on the same surface. The NDT and ICP methods are collectively called dense point methods because they consider all points in the registration; their results are easily influenced by those points on different sides of the tree stems. The NDT algorithm considers the distribution of all points in the overlap, and the ICP algorithm achieves the registration based on the minimization of the distances between matching points. Although the ICP algorithm cannot achieve accurate registration results, the influence in the low-overlap region can be reduced by iterative optimization, which is difficult for the NDT algorithm. As a result, the distance deviations from NDT are larger than those of the ICP algorithm. In addition, the deviations of the NDT and LOAM methods were approximately equal in the plots (see Table 7) and corresponded to the visual performances in Table 6. LOAM is a sparse feature method that combines line and plane features for LiDAR odometry, and it generally requires a fine initial transformation between point clouds. Although only a few features are required by

the method, the inaccurate corresponding pairs in the low-overlap region make the method fall into a local minimum. Because the initial transformation was provided by the NDT method, the worst accuracy results were similar. The results of the proposed method show a vast overall improvement in the two plots. The mean deviations of the distances between the detected trees and the reference decrease to approximately 0.01 m (in plot A1) and even millimeters (in plot A2). The most significant improvement is larger than an order of magnitude decrease in the standard deviations of the distances between the detected trees and the reference.

Table 8 shows the mapping accuracy of the proposed method and the NDT, ICP, and LOAM methods in the vertical direction. First, we manually select some remarkable, stable feature points from the ground and branches in the MLS point cloud and their corresponding points in the TLS data; then, the vertical distance deviations between the corresponding pairs are calculated. From Table 8, the deviations obtained by the four methods are small and approximate in the plots, of which the mean deviations vary between 0.01 m and 0.02 m, the standard deviations are approximately 0.01 m, and the maximum deviation is less than 0.05 m. The ground provided strong constraints, so the NDT and ICP methods, which achieve registration based on the whole points, obtain accurate registration results in the vertical direction. The proposed method and the LOAM method achieve registration based on some features, and their initial transformations between the MLS data and the single-scan TLS data are provided by the NDT method, so after nonlinear optimization, the vertical deviations from the two methods are close to the results from the NDT method.

Table 8

Vertical accuracy of different methods.

Plots	Methods	Points	Vertical deviations		
		N_P	Mean (m)	STD (m)	Max (m)
Plot A1	NDT	15	0.0220	0.0148	0.0440
	LOAM	15	**0.0178**	0.0156	0.0487
	ICP	15	0.0206	0.0136	0.0419
	The proposed method	15	0.0180	**0.0096**	**0.0366**
Plot A2	NDT	15	0.0150	0.0078	**0.0285**
	LOAM	15	0.0207	0.0122	0.0487
	ICP	15	0.0140	**0.0076**	0.0287
	The proposed method	15	**0.0117**	0.0087	0.0351

Overall, the results of the proposed method are more reliable than the results of the other three methods. Due to weak constraint, registration errors of the NDT, ICP, and LOAM methods are mainly in the horizontal direction. The proposed method is highly dependent on virtual features and real features, especially the virtual features. In the process of motion estimation, the virtual features effectively decrease the errors in tree stem locations that exist in the other three methods by providing a constraint between the center and the surface of the tree stem; meanwhile, the real features retain the overall accuracy of the LiDAR odometry.

5. Conclusions

LiDAR-based forest mapping is a significant method for obtaining precise forestry inventories. To achieve complete and fast forest mapping, this paper proposed a novel method combining the single-scan TLS and MLS systems for forest measurements. Meanwhile, comprehensive experiments were performed to verify the feasibility and effectiveness of the proposed method, and a good result was obtained. In the data acquisition phase, the proposed method acquired more complete data than the single-scan TLS method, and the efficiency is higher than that of the multi-scan TLS method. In the forest mapping phase, the single-scan TLS point cloud provided a strong global consistency constraint for the MLS-based SLAM technique and maintained positioning accuracies without a GNSS-

IMU system. Moreover, in the case without loop-closure detection, the proposed method still achieved accurate forest mapping. In addition, a new point cloud registration method for combining the virtual features and the real features specific to forest environments was proposed by the paper. The method effectively solved the inaccurate registration problem caused by insufficient overlap and inaccurate corresponding pairs, for which the virtual features played an important role in reducing the horizontal errors. Compared to other classic methods, the registration results of the proposed method were also more accurate.

As an aerial platform, the UAV-LiDAR system (ULS) can obtain structural information below the canopy that approximates that obtained by the TLS system. Moreover, the ULS is more efficient than the TLS system, and the information from above the canopy is more complete. As a result, the ULS is increasingly being used more widely in recent years. In the future, therefore, to achieve fast and complete data acquisition in large-scale forest plots, the ULS and MLS will be combined for forest mapping based on the proposed method.

Acknowledgements

This work was supported by the National Natural Science Foundation of China, grant nos. 41671414, 41971380, 41331171 and 41171265. This work was also supported by the National Key Research and Development Program of China (no. 2016YFB0501404).

References

Astrup, R., Ducey, M.J., Granhus, A., Ritter, T., von Lüpke, N., 2014. Approaches for estimating stand-level volume using terrestrial laser scanning in a single-scan mode. Can. J. For. Res. 44, 666–676.

Behzadian, B., Agarwal, P., Burgard, W., Tipaldi, G.D., 2015. Monte Carlo localization in hand-drawn maps. In Proc. of the IEEE/RSJ International Conference on Intelligent Robots and Systems (IROS).

Besl, P.J., Mckay, N.D., 1992. A method for registration of 3-D shapes. IEEE T. Pattern Anal. 14, 239-256.

Calders, k., Armston, J., Newnham, G., Herold, M., Goodwin, N., 2014. Implications of sensor configuration and topography on vertical plant profiles derived from terrestrial LiDAR. Agric. For. Meteorol. 194, 104–117.

Cifuentes, R., Zande, D.V. der, Farifteh, J., Salas, C., Coppin, P., 2014. Effects of voxel size and sampling setup on the estimation of forest canopy gap fraction from terrestrial laser scanning data. Agric. For. Meteorol. 194, 230–240.

Dissanayake, M.W.M.G., Newman, P., Clark, S., Durrant-Whyte, H.F., Csorba, M., 2001. A solution to the simultaneous localization and map building (SLAM) problem. IEEE Transactions on Robotics and Automation 17(3), 229-241.

Grisetti, G., Kummerle, R., Stachniss, C., Burgard, W., 2010. A tutorial on graph-based SLAM. IEEE Intelligent Transportation Systems Magazine 2, 31-43.

Grisetti, G., Stachniss, C., Burgard, W., 2007. Improved techniques for grid mapping with rao-blackwellized particle filters. IEEE Trans. Robot. 23, 34-46.

Hess, W., Kohler, D., Rapp, H., Andor, D., 2016. Real-time loop closure in 2D LiDAR SLAM. IEEE International Conference on Robotics and Automation (ICRA).

Henning, J. G., Radtke, P. J., 2006. Detailed stem measurements of standing trees from ground-based scanning lidar. Forest Sci. 52(1), 67-80.

Hilker, T., Coops, N.C., Culvenor, D.D., Newnham, G., Wulder, M.A., Bater, C.W., Siggins, A., 2012. A simple technique for co-registration of terrestrial LiDAR observations for forestry applications. Remote Sens. Lett. 3, 239-247.

Hyyppä, J., 2000. Feasibility for estimation of single tree characteristics using laser scanner. International Geoscience and Remote Sensing Symposium 3, 981-983.

Javanmardi, M., Javanmardi, E., Gu, Y., Kamijo, S., 2017. Towards high-definition 3D urban mapping: road feature-based registration of mobile mapping systems and aerial imagery. Remote Sens. 9, 975.

Kelbe, D., Aardt, J.V., Romanczyk, P., Leeuwen, M.V., Cawse-Nicholson, K., 2016. Marker-free registration of forest terrestrial laser

scanner data pairs with embedded confidence metrics. IEEE Trans. Geosci. Remote Sens. 54, 4314-4330.

Kohlbrecher, S., Von Stryk, O., Meyer, J., Klingauf, U., 2011. A flexible and scalable SLAM system with full 3D motion estimation. IEEE International Symposium on Safety, Security, and Rescue Robotics.

Konolige, K., Grisetti, G., Kümmerle, R., Limketkai, B., Vincent, R., 2010. Efficient sparse pose adjustment for 2D mapping. In Proc. of Int. Conf. on Intelligent Robots and Systems (IROS).

Kukko, A., Kaijaluoto, R., Kaartinen, H., Lehtola, V.V., Jaakkola, A., Hyyppä, J., 2017. Graph SLAM correction for single scanner MLS forest data under boreal forest canopy. ISPRS J. Photogramm. Remote Sens. 132, 199-209.

Kümmerle, R., Steder, B., Dornhege, C., Kleiner, A., Grisetti, G., Burgard, W., 2011. Large scale graph-based SLAM using aerial images as prior information. Autonomous Robots 30, 25-39.

Labbé, M., Michaud, F., 2014. Online global loop closure detection for large-scale multi-session graph-based SLAM. In Proc. of the IEEE/RSJ International Conference on Intelligent Robots and Systems.

Latifi, H., Fassnacht, F.E., Müller, J., Tharani, A., Dech, S., Heurich, M., 2015. Forest inventories by LiDAR data: A comparison of single tree segmentation and metric-based methods for inventories of a heterogeneous temperate forest. International Journal of Applied Earth Observations and Geoinformation. 42, 162–174.

Liang, X., Hyyppä, J., Kukko, A., Kaartinen, H., Jaakkola, A., Yu, X., 2014. The use of a mobile laser scanning system for mapping large forest plots. IEEE Geosci. Remote Sens. Lett. 11, 1504-1508.

Liang, X., Kankare, V., Hyyppä, J., Wang, Y., Kukko, A., Haggrén, H., Yu, X., Kaartinen, H., Jaakkola, A., Guan, F., Holopainen, M., Vastaranta, M., 2016. Terrestrial laser scanning in forest inventories. ISPRS J. Photogramm. Remote Sens. 115, 63-77.

Liang, X., Kukko, A., Hyyppä, J., Lehtomäki, M., Pyörälä, J., Yu, X., Kaartinen, H., Jaakkola, A., Wang, Y., 2018. In-suit measurements from mobile platforms: an emerging approach to address the old challenges associated with forest inventories. ISPRS J. Photogramm. Remote Sens. 143, 97-107.

Liang, X., Litkey, P., Hyyppä, J., Kaartinen, H., Vastaranta, M., Holopainen, M., 2012. Automatic stem mapping using single-scan terrestrial laser scanning. IEEE Trans. Geosci. Remote Sens. 50, 661–670.

Lovell, J.L., Jupp, D.L.B., Newnham, G.J., Culvenor, D.S., 2011. Measuring tree stem diameters using intensity profiles from ground-based scanning lidar from a fixed viewpoint. ISPRS J. Photogramm. Remote Sens. 66, 46–55.

Magnusson, M., Lilienthal, A., Duckett, T., 2007. Scan registration for autonomous mining vehicles using 3D-NDT. Journal of Field Robotics 24, 803-827.

Mouragnon, E., Lhuillier, M., Dhome, M., Dekeyser, F., Sayd, P., 2009. Generic and real-time structure from motion using local bundle adjustment. Image and Vision Computing 27(8), 1178-1193.

Maas, H.G., Bienert, A., Scheller, S., and Keane, E., 2008. Automatic forest inventory parameter determination from terrestrial laser scanner data. Int. J. Remote Sens. 29, 1579–1593.

Mitra, N.J., Gelfand, N., Pottmann, H. and Guibas, L., 2004, July. Registration of point cloud data from a geometric optimization perspective. In *Proceedings of the 2004 Eurographics/ACM SIGGRAPH symposium on Geometry processing* (pp. 22-31). ACM.

Mellado, N., Aiger, D. and Mitra, N.J., 2014, August. Super 4pcs fast global pointcloud registration via smart indexing. In *Computer Graphics Forum* (Vol. 33, No. 5, pp. 205-215).

Mengesha, T., Hawkins, M., Nieuwenhuis, M., 2015. Validation of terrestrial laser scanning data using conventional forest inventory methods. Eur J Forest Res. 134, 211-222.

Mielle, M., Magnusson, M., Lilienthal, A.J., 2018. A method to segment maps from different modalities using free space layout MAORIS: MAp Of RIpples Segmentation. In Proc. of the IEEE International Conference on Robotics and Automation (ICRA).

Mur-Artal, R., Montiel, J.M.M., Tardós, J.D., 2015. ORB-SLAM: a versatile and accurate monocular SLAM system. IEEE T. ROBOT. 31, 1147-1163.

Murphy, G.E., Acuna, M.A., Dumbrell, T., 2010. Tree value and log product yield determination in radiate pine (Pinus radiate) plantations in Australia: comparisons of terrestrial laser scanning with a forest inventory system and manual measurements. Can. J. For. Res. 40, 2223-2233.

Næsset, E., 2011. Estimating above-ground biomass in young forests with airborne laser scanning. International Journal of Remote Sensing. 32, 473–501.

Newnham, G.J., Armston, J.D., Calders, K., Disney, M., Lovell, J., Schaaf, C.B., Strahler, A.H., Danson, F.M., 2015. Terrestrial laser scanning for plot-scale forest measurement. Current Forestry Reports 1, 239-251.

Polewski, P., Yao, W., Heurich, M., Krzystek, P., Stilla, U., 2017. A voting-based statistical cylinder detection framework applied to fallen tree mapping in terrestrial laser scanning point clouds. ISPRS J. Photogramm. Remote Sens. 129, 118-130.

Polewski, P., Yao, W., Cao, L., Gao, S., 2019. Marker-free coregistration of UAV and backpack LiDAR point clouds in forested areas. ISPRS J. Photogramm. Remote Sens. 147, 307-318.

Pomerleau, F., Colas, F. and Siegwart, R., 2015. A review of point cloud registration algorithms for mobile robotics. *Foundations and Trends® in Robotics*, *4*(1), pp.1-104.

Pueschel, P., 2013. The influence of scanner parameters on the extraction of tree metrics from FARO Photon 120 terrestrial laser scans. ISPRS J. Photogramm. Remote Sens. 78, 58-68.

Rusu, R.B., Blodow, N., Marton, Z.C. and Beetz, M., 2008, September. Aligning point cloud views using persistent feature histograms. In *2008 IEEE/RSJ International Conference on Intelligent Robots and Systems* (pp. 3384-3391). IEEE.

Shah, D.C., Campbell, M.E., 2013. A qualitative path planner for robot navigation using human-provided maps. The International Journal of Robotics Research 32, 1517-1535.

Shao, J., Zhang, W., Mellado, N., Grussenmeyer, P., Li, R., Chen, Y., Wan, P., Zhang, X., Cai, S., 2019. Automated markerless registration of point clouds from TLS and structured light scanner for heritage documentation. J. Cult. Herit. 35, 16-24.

Spies, T. A., 1998. Forest structure: a key to the ecosystem. Northwest Science 72, 34-39.

Stovall, A.E.L., Vorster, A.G., Anderson, R.S., Evangelista, P.H., Shugart, H.H., 2017. Non-destructive aboveground biomass estimation of coniferous trees using terrestrial LiDAR. Remote Sens. Environ. 200, 31-42.

Theiler, P.W., Wegner, J.D. and Schindler, K., 2014-1. Fast registration of laser scans with 4-point congruent sets-what works and what doesn't. *ISPRS annals of the photogrammetry, remote sensing and spatial information sciences*, *2*(3), p.149.

Theiler, P.W., Wegner, J.D., Schindler, K., 2014-2. Keypoint-based 4-points congruent sets – automated marker-less registration of laser scans. ISPRS J. Photogramm. Remote Sens. 96, 149-163.

Torresan, C., Chiavetta, U., Hackenberg, J., 2018. Applying quantitative structure models to plot-based terrestrial laser data to assess dendrometric parameters in dense mixed forests. Forest Systems 27, 1-15.

Trochta, J., Kral, K., Janik, D., Adam, D. 2013. Arrangement of terrestrial laser scanner positions for area-wide stem mapping of natural forests. Can. J. For. Res. 43, 355-363.

Wang, C., Hou, S., Wen, C., Gong, Z., Li, Q., Sun, X., Li, J., 2018. Semantic line framework-based indoor building modeling using backpacked laser scanning point cloud. ISPRS J. Photogramm. Remote Sens. 143, 150-166.

Wilkers, P., Lau, A., Disney, M., Calders, K., Burt, A., Gonzalez de Tanago, J., Bartholomeus, H., Brede, B., Herold, M., 2017. Data acquisition considerations for terrestrial laser scanning of forest plots. Remote Sens. Environ. 196, 140-153.

Zhang, J., Singh, S., 2014. LOAM: lidar odometry and mapping in real-time. Robotics: Science and Systems Conference.

Zhang, W., Chen, Y., Wang, H., Chen, M., Wang, X., Yan, G., 2016a. Efficient registration of terrestrial LiDAR scans using a coarse-to-fine strategy for forestry applications. Agric. For. Meteorol. 225, 8-23.

Zhang, W., Qi, J., Wan, P., Wang, H., Xie, D., Wang, X., Yan, G., 2016b. An easy-to-use airborne LiDAR data filtering method based on cloth simulation. Remote Sens. 8, 501.

Zhang, W., Wan, P., Wang, T., Cai, S., Chen, Y., Jin, X., Yan, G., 2019. A novel approach for the detection of standing tree stems from plot-level terrestrial laser scanning data. Remote Sens. 11(2), 211.